



Experimental and numerical analyses on working performance of a high arch dam with deep-seated joints: Yebatan arch dam, China

Wen Zhang¹ · Yuan Chen¹ · Bao-quan Yang¹  · Lin Zhang¹ · Chong Zhang² · Xiao-qiang Liu²

Received: 21 June 2018 / Accepted: 11 January 2019 / Published online: 4 February 2019
© Saudi Society for Geosciences 2019

Abstract

High arch dams commonly face complicated geological conditions at the dam site, which is particularly prominent in numerous projects in the southwest mountainous area of China. The deep-seated joint is a special geological defect caused by unloading fracturing of the deep rock mass, which is unfavourable to the working performance of high arch dam projects. The Yebatan arch dam is a world-class high arch dam, situated in a deeply carved V-shaped gorge with deep-seated joint zones in both banks. In this paper, both geomechanical model test and numerical analysis are carried out to study the working performance of the Yebatan arch dam and abutment, which are affected by the deep-seated joint zones. The research results demonstrate that the deep-seated joint zones have a significant effect on the arch dam and abutment working performance. It is highly dependent on the location of the class IV_S strong relaxed rock mass and the combination with faults. The class IV_S strong relaxed rock mass in the left abutment has a great impact on the deformation of arch dam and abutment, and fault f29 (f74) plays a dominant role in controlling the anti-sliding stability of the right abutment. Subsequently, a kind of concrete replacement measure is proposed in order to treat these project weaknesses. The additional numerical analysis results indicate the deformation and stability performance of arch dam and abutment are greatly improved after reinforced. The reinforcement measure is effective for Yebatan project.

Keywords Deep-seated joint · Geomechanical model test · Numerical analysis · Yebatan arch dam · Working performance · Reinforcement measure

Introduction

With the continual development of hydropower projects, high arch dam has gradually become one of the main dam types for large-scale hydropower station projects globally (Hennig et al. 2013; Song et al. 2015). Compared to other dam types, arch dam offers the advantages of superior economy and higher overloading capacity. However, a high arch dam has more stringent geological condition demands, owing to the high structural stability and engineering safety requirements (Ren et al. 2012). Numerous high arch dams have been built in the

southwest alpine valley areas of China, with some still under construction at present (Wang et al. 2013; Zhu et al. 2015; Yin et al. 2015). Most of these high arch dams are situated in high mountain valleys with complicated geological conditions (Pan and He 2000). The stability and safety of arch dam and abutment have always been of concern (Zhang et al. 2015). The deep-seated joint is one of the typical adverse geological structures developed within the steep slopes and caused by the unloading fracturing of the deep rock mass (Lan et al. 2004; Song et al. 2011). As the deep-seated joints can reduce the rock mass integrity and strength, its technical treatment issue should be carefully considered during the project design and construction periods.

The deep-seated joint has brought various adverse effects in many projects. The Bearegard arch dam in Aosta Valley, Italy, has a deep-seated joint zone of up to 20 m in the left abutment slope. The deep-seated joint zone caused a continuous slope movement, resulting a landslide hazard (Barla et al. 2010). The Jinping I arch dam in the Yalong River, China, has encountered the problem of deep-seated joints in the left abutment. The strike directions of these deep-seated joints are

✉ Bao-quan Yang
yangbqscu1019@163.com

¹ State Key Laboratory of Hydraulics and Mountain River Engineering, College of Water Resources and Hydropower, Sichuan University, Chengdu 610065, China

² Power China Chengdu Engineering Corporation Limited, Chengdu 610065, China

parallel to the slope, which is particularly disadvantageous to the left abutment stability (Lin et al. 2018). These project cases show that the deep-seated joint is a hidden danger for dam projects. A great attention should be paid to study its impact and the treatment measures.

The Yebatan arch dam is a world-class high arch dam located in southwest China. At the dam site, the deep-seated joint zones are developed in both abutments. To ensure project stability and safety, it is necessary to study the effects of the deep-seated joint zones on the working performance of arch dam and abutment. At present, geomechanical model test and numerical analysis are the most common and effective methods for these issues (Li et al. 2005; Lin et al. 2014; Liu et al. 2017a). The geological structures of abutments, such as rock masses, faults and joints, can be factually modelled in the geomechanical model test. Moreover, the physical and mechanical characteristics of these geological structures can also be similarly simulated. Through the destructive experiment, the deformation characteristics, failure process and failure patterns of arch dam and abutment on complicated foundation can be determined. By analysing the results, the working performance of arch dam and abutment can be evaluated, and the project weaknesses can also be revealed, which provide a reference for reinforcement design. Numerical analysis provides another convenient solution for complicated engineering problems. Current numerical methods for evaluating the working performance of arch dams and abutments include the finite element method (FEM), limit equilibrium method (LEM) and distinct element method (DEM) (Zhou et al. 2008a; Sun et al. 2011; Guo et al. 2011). The numerical analysis can simulate different load conditions and the calculation can be repeated, which can save a lot of resources, such as manpower and financial power. Moreover, it can provide more detailed analysis results of the structure. Combining these two methods, many complex engineering problems can be analysed to get more comprehensive and reliable research results.

In this study, both methods are adopted to focus on the effects of the deep-seated joint zones on the Yebatan arch dam and abutment working performance. Firstly, the working performance of arch dam and abutment under the effect of the deep-seated joint zones is studied. Through model test and numerical analysis, the deformation characteristics and failure patterns are obtained, and the abutment weaknesses are revealed. Thereafter, the effect degree of the deep-seated joint zones is discussed based on the research results, and a kind of reinforcement measure is proposed. Finally, the working performance of arch dam and abutment under the reinforced condition is further studied by another numerical analysis. By comparing the deformation characteristics, stress distribution and failure patterns prior to and after reinforcement, the reinforcement effectiveness is evaluated.

Geological conditions

The Yebatan arch dam is located in the upper reaches of the Jinsha River, at the junction of the Yunnan and Sichuan provinces. The dam site is situated about 600 m downstream of the confluence of the Jinsha River and the Jiangu River (illustrated in Fig. 1). It is a hydropower project with the largest installed capacity in the upper reaches of the Jinsha River. The main project task is composed of power generation, flood prevention and environmental protection. The concrete double-curvature arch dam is 217 m high, with a normal water level of EL. 2889 m.

The dam site is situated in a deeply carved V-shaped gorge, with high and steep slopes (see Fig. 2). The riverbed is straight at the dam site, and the slope angles of the left and right banks are approximately 40°–50° and 40°–55°, respectively, which indicates that the valley shape is basically symmetrical. The rock lithology of the dam foundation is relatively unitary, and the rock mass is mainly composed of quartz diorite (Liu et al. 2017b).

Geological defects, such as faults, joints and deep-seated joints, are developed in the dam site. The valley evolution is accompanied by a strong crust uplift, resulting in high in situ stress in the dam site. The maximum principal stress direction is basically orthogonal to the water flowing direction. Owing to the strong down-cutting effect of the rivers, the in situ stress is released within the valley slopes, and two strip zones of the deep-seated joints are formed inside both banks (as illustrated in Fig. 3). The deep-seated joints are mainly characterised by several gapped cracks or broken zones filled with detritus. Moreover, the class IV_S strong relaxed rock masses (shadow zones in Fig. 3) on both banks are located in transmission direction of the arch thrust and near the arch abutment. This is a hidden danger for this hydropower project. Additionally, the faults also develop severely in both abutments. The two abutments are cut by these weak structural planes, which decrease the integrity and weaken the bearing capacity of the rock mass.

These geological defects, especially the deep-seated joints, are particularly disadvantageous to the Yebatan hydropower project. Deep-seated joints may increase the arch dam and abutment deformation owing to the poor mechanical properties (displayed in Table 1). And the faults may produce a wide failure zone and affect the abutment stability. The working performance of the project may be greatly affected, and further investigation is required. The main physical-mechanical parameters of faults are listed in Table 2.

Methods

Geomechanical model test scheme

The geomechanical model test is a nonlinear destructive test based on the model similarity theory. It must meet the

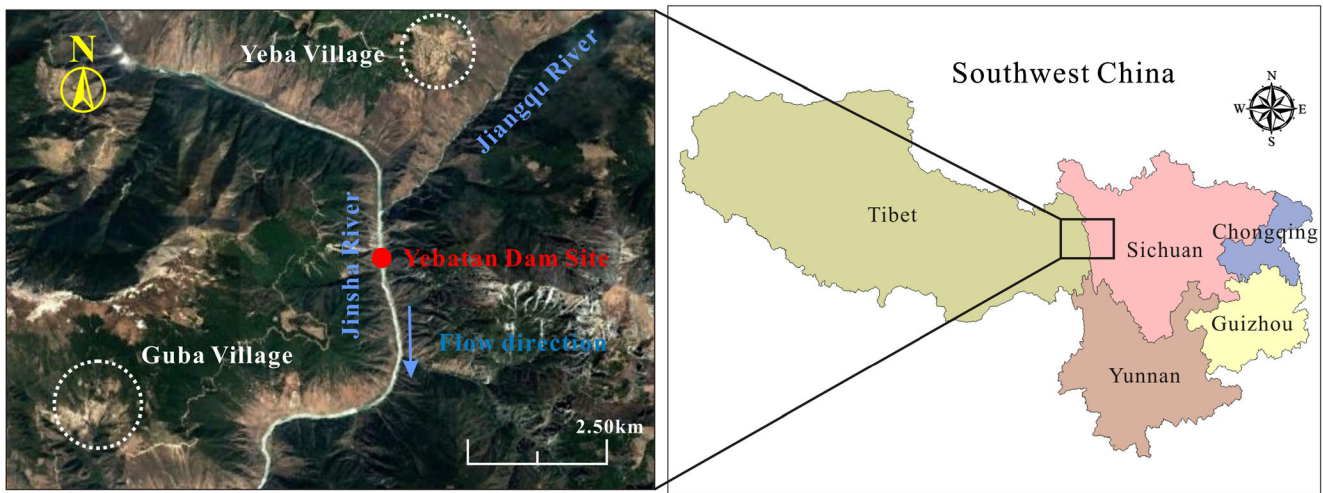


Fig. 1 Location of Yebatan arch dam

similarity requirements between the prototype and model (Fei et al. 2010; Zhu et al. 2010; Chen et al. 2012). According to the simulation principles, the most critical similarity relations are as follows:

$$C_L = C_E = C_c \tag{1}$$

$$C_\gamma = C_\varepsilon = C_\mu = C_f \tag{2}$$

$$C_F = C_\gamma C_L^3 \tag{3}$$

where C_L , C_E , C_γ , C_ε , C_μ , C_c , C_f and C_F are the similarity coefficients of the geometry, Young’s modulus, unit weight, strain, Poisson’s ratio, cohesive strength, friction coefficient and load, respectively (Fumagalli 1973; Zuo 1984). Each

similarity coefficient is defined as the ratio of the prototype parameter to model parameter. In this study, C_L is selected to be 200, while C_γ is equal to 1.0. The other similarity coefficients can be calculated by similarity relations (1)–(3), which are displayed in Table 3.

The simulated model range extends approximately 0.7, 2.4 and 1.8 times the dam height from the dam position control point to upstream, downstream and both banks, respectively, which is sufficient to include the main geological structures. As $C_L=200$, the geomechanical model size is 3.93 m × 3.30 m (across the river × along the river), and the model thickness is 10 cm. Considering the complicated dam site geological conditions, the geological structures of the two abutments, except the deep-seated joint zones, are

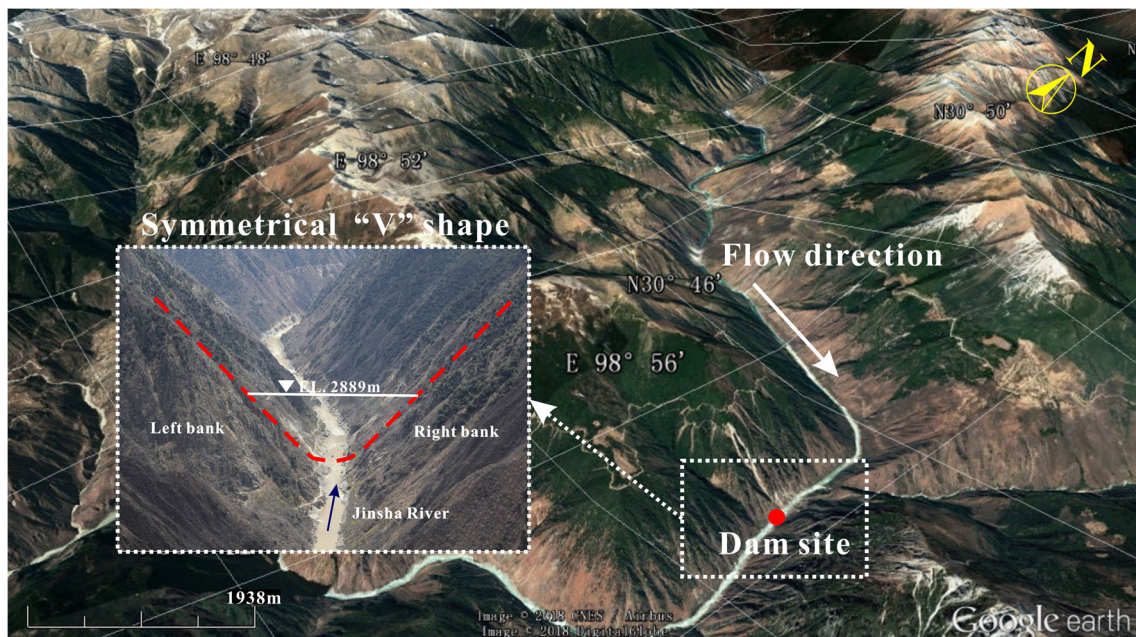


Fig. 2 Geomorphological conditions of Yebatan hydropower project as seen on Google Earth

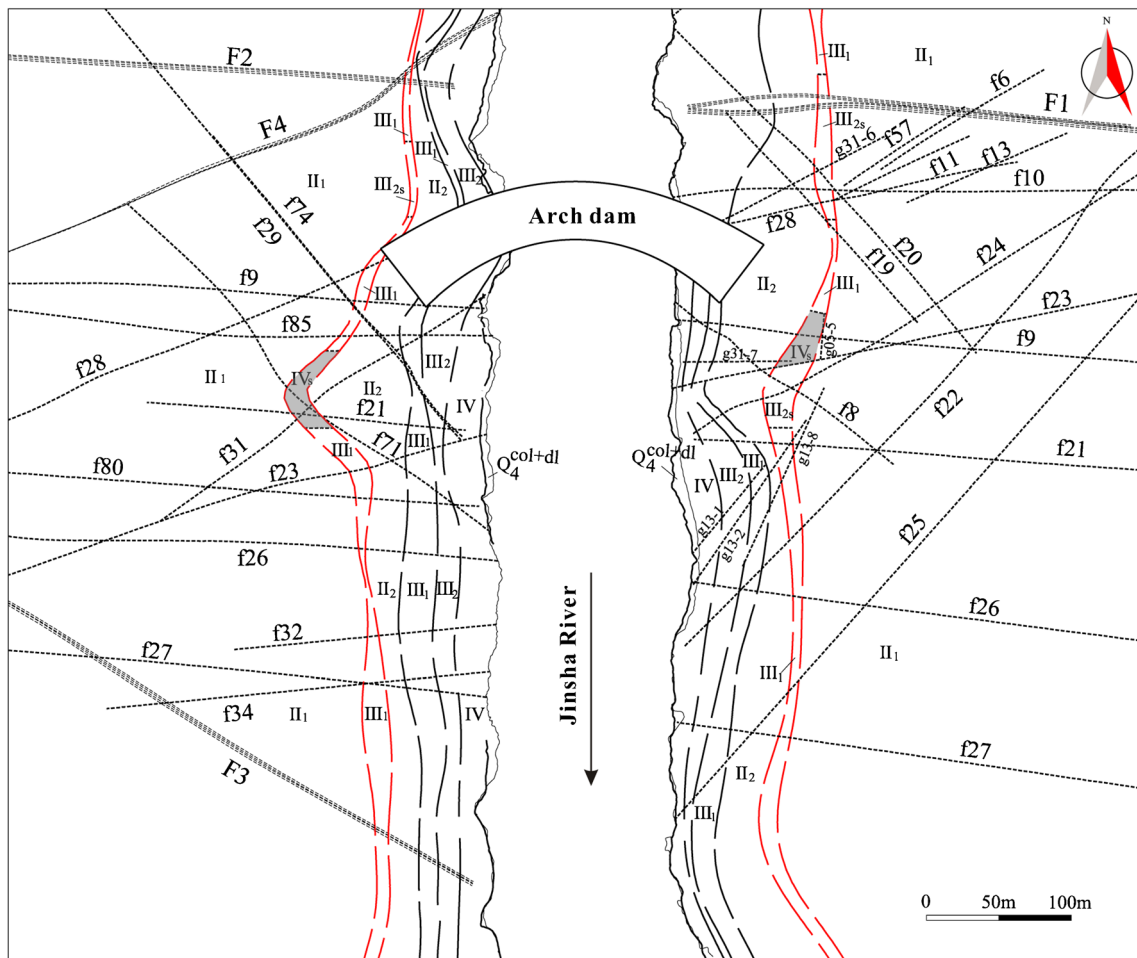


Fig. 3 Geological horizontal section of Yebatan project at EL. 2750 m (red line areas indicate deep-seated joint zones)

appropriately generalised. As illustrated in Fig. 4, two deep-seated joint zones, seven classes of rock masses, main faults and joints J1, J2 and J3 are experimentally simulated. The geomechanical model is depicted in Fig. 5a.

The experimental materials are composed of different mixture proportions of baryte powder, gypsum, cement, water and other additives. Based on the similarity coefficients, the material mechanical parameters used in the geomechanical model are listed in Table 4. The arch dam is modelled by pouring. Small block masonry technology is employed in this

experiment (Liu et al. 2013). The small rhombic blocks are used to build the rock masses (as illustrated in Fig. 5b). In order to simulate joints J1, J2 and J3, these rhombic blocks are staggered arranged. The shear strength of the faults is simulated by a type of soft model material and various thin films with different roughness, which are set between the rock blocks. It is worth noting that the small rhombic blocks used for the class IV_S strong relaxed rock mass are further cut into smaller pieces in order to simulate the broken and weak structure characteristics.

Table 1 Physical-mechanical parameters of rock mass

Rock masses	Density (g/cm ³)	Young's modulus (GPa)	Poisson's ratio	Cohesion (MPa)	Friction coefficient
II ₁	2.70–2.75	14.0–23.0	0.20–0.23	1.70	1.28
II ₂	2.70–2.75	12.0–19.0	2.60–2.70	1.20	1.20
III ₁	2.60–2.70	11.0–13.0	0.25–0.27	1.10	1.08
III ₂	2.60–2.70	8.0–10.0	0.27–0.30	0.90	0.95
III _{2s}	2.60–2.70	3.0–4.0	2.60–2.70	0.85	0.86
IV	2.50–2.60	2.0–3.0	0.33–0.35	0.60	0.70
IV _S	2.60–2.70	1.0	0.33–0.35	0.50	0.60

Table 2 Physical-mechanical parameters of main faults

Faults	Occurrence	Width (m)	Young's modulus (GPa)	Cohesion (MPa)	Friction coefficient
f24	N50–60°E/NW∠70–85°	0.1–0.2	1.0	0.01	0.35
f22	N30–35°E/NW∠75–85°	0.4–0.8	1.4	0.05	0.40
f29	N40–50°W/NE∠65–75°	0.2–0.6	1.4	0.01	0.35
f74	N40–50°W/NE∠70–80°	0.1–0.2	1.4	0.05	0.40
f71	N60–65°W/NE∠30–35°	0.2–0.7	2.0	0.10	0.50
f28	N60–70°E/NW∠75–85°	0.4–0.7	1.4	0.01	0.35
f31	N50–60°E/NW∠70–85°	0.4–0.6	1.4	0.05	0.40
f85	EW/S∠55–60°	0.1–0.3	1.4	0.05	0.40
f23	N70–75°E/NW∠75–85°	0.4–0.8	1.0	0.01	0.35
f21	EW/S∠55–60°	0.1–0.4	1.4	0.05	0.40
f9	EW/S∠55–60°	0.1–0.15	1.4	0.05	0.40

The experimental facilities mainly include a loading system and a displacement measuring system. The gravity and the upstream water pressure loads are simulated experimentally. The gravity is simulated by the model materials using $C_L = 1.0$, while the upstream water load is applied by oil jacks (illustrated in Fig. 5c). To measure the arch dam and abutment displacement, a number of measuring points are installed at the arch dam and abutment surface, especially at the class IV_S strong relaxed rock mass in the left and right deep-seated joint zones. The displacements are captured by the displacement sensors, which are installed at each measuring point along and across the river. The displacement values are displayed by the displacement digital display instrument (depicted in Fig. 5d).

The overloading method is adopted in this geomechanical model test, which can reflect the impact of excessive floods on the stability of dams (Zhou et al. 2008b; Zhang et al. 2009; Yang et al. 2015). The overloading factor K_P is defined as the load P to the normal load P_0 (Chen et al. 2015). In this study, a step-loading procedure is performed during the overloading test, and the entire loading process can be summarised as follows. Firstly, minor loads are applied to preload the model. Secondly, the load is increased to P_0 to simulate the action of a normal water load. Finally, a step-loading process is performed with an incremental load of $0.2P_0$ until the model fails. The displacement and failure process of the model are the main monitoring targets during the test. The displacement values at each load step are recorded and the model failure patterns are observed.

Numerical analysis

A numerical analysis based on a nonlinear FEM is conducted correspondingly, offering additional perspectives for studying the effects of deep-seated joint zones on the working performance of arch dam and abutment in detail. ANSYS is a large commercial FEM software, which is commonly adopted for analysing the engineering problems of high arch dam projects. A FEM calculation model (illustrated in Fig. 6) is designed in

the ANSYS software. The FEM model simulation range is the same as that of the geomechanical model. And the numbers of elements and nodes are 20,307 and 27,869, respectively.

The simulation scheme of the geological structures used in the experiment is adopted in the FEM calculation, and the mechanical parameters of each material of the FEM model are equal to the prototype values. The FEM calculation is based on the elastoplastic constitutive theory and Drucker-Prager (D-P) yield criterion. The D-P yield criterion is a pressure-dependent model used to determine whether the material trends to plastic yield. The Drucker-Prager yield criterion can be expressed by the following forms (Alejano 2012; Drucker and Prager 2013):

$$f(I_1, \sqrt{J_2}) = \sqrt{J_2} - BI_1 - A = 0 \tag{4}$$

$$I_1 = \sigma_1 + \sigma_2 + \sigma_3 \tag{5}$$

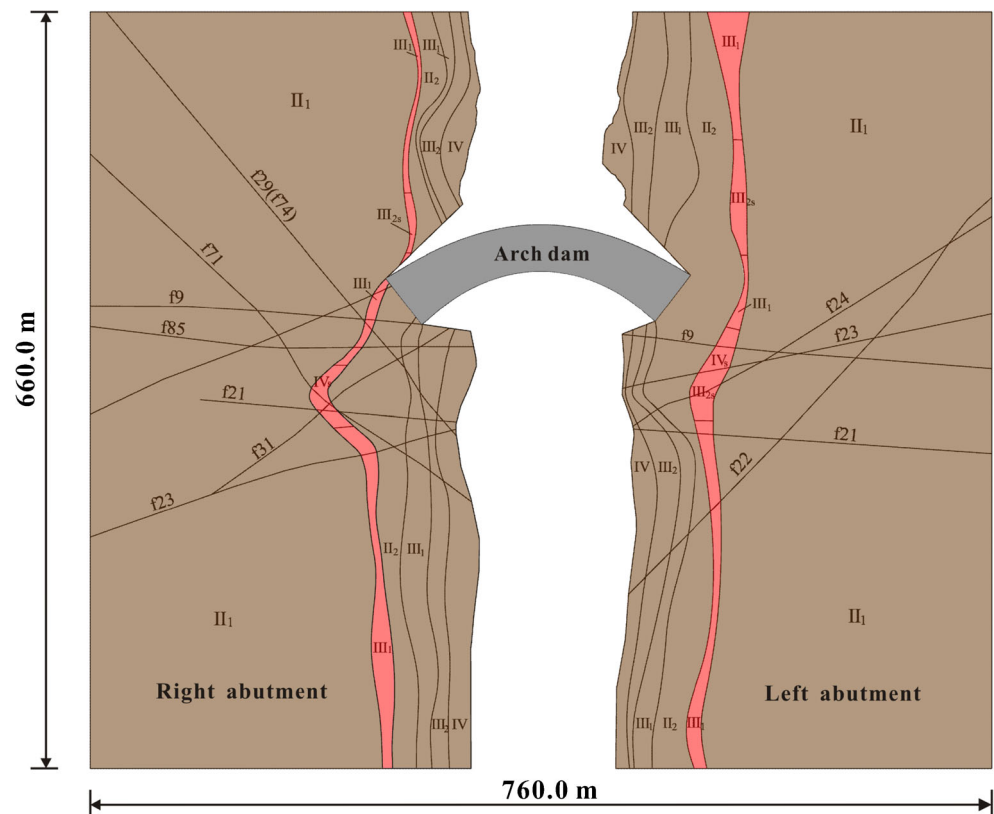
$$J_2 = \frac{1}{6} [(\sigma_2 - \sigma_3)^2 + (\sigma_2 - \sigma_1)^2 + (\sigma_3 - \sigma_1)^2] \tag{6}$$

where I_1 is the first invariant of the Cauchy stress, J_2 is the second invariant of the deviatoric part of the Cauchy stress, and A and B are constants expressed in terms of the cohesion (c) and the angle of internal friction (φ). For using the D-P yield criterion in ANSYS, the parameters of c and φ need to be set for the material. Due to the advantage of convenient calculation and easy convergence, the D-P yield criterion has been widely applied to the pressure-dependent materials in numerical analysis. The arch dam concrete element type is SOLID65 and the rock mass is SOLID45. The element constraints at the upstream and downstream boundaries, the left and right boundaries and the bottom surface are in the directions of the

Table 3 Similarity coefficients of geomechanical model test

C_L	C_E	C_γ	C_ε	C_μ	C_c	C_f	C_F
200	200	1	1	1	200	1	200 ³

Fig. 4 Schematic of simulated arch dam and geological structures (red area represents deep-seated joint zone)



Y , X - and Z -axes, respectively. In order to maintain consistency with the load case simulated in the geomechanical model test, the gravity and upstream water loads are also considered in the FEM calculation. The loads applied in the FEM model are progressively simulated in the following scheme. The gravity of the concrete arch dam and the abutment is applied additively to the first step. Thereafter, the upstream water load is applied on the upstream face of the arch dam, as in the case of the normal water load. Next, $0.2P_0$ is set as a load increment, until $4P_0$ is applied. Certain analysis results of the FEM model at each load step can be obtained in the form of contour plots in the post-processing module of the ANSYS software.

Results

Deformation characteristics under normal water load

Figure 7 illustrates the arch dam displacement distribution. In this figure, the displacement along the river is greater than that across the river. Furthermore, the maximum displacement along the river occurs at the arch crown, while the arch abutments exhibit the largest displacement across the river. This implies that the arch dam displacement conforms to the general rules. In addition, the displacement distribution of the two half arches is basically the same, which indicates that the arch dam deformation exhibits strong symmetry.

The abutment displacement distribution characteristics are as follows: the displacements of the left and right abutments are the largest near the arch abutment and gradually decrease towards the downstream. Moreover, the displacements of area A (between fault f29 (f74) and the right arch abutment) and area B (enclosed by the left arch abutment, deep-seated joint zone and fault f24) are the largest of the two abutments (as illustrated in Fig. 8). Analysing the displacement values of the two abutments, it can be observed that the deformation is relatively small. Moreover, the displacements near the two arch abutments are nearly the same, indicating that the abutment deformation is symmetric under a normal water load.

The displacements of the deep-seated joint zones in both abutments exhibit certain differences. The largest displacement of the deep-seated joint zone in the left abutment appears in the class IV_S strong relaxed rock mass, and the largest displacement of the deep-seated joint zone in the right abutment is between fault f29 (f74) and the right arch abutment. Moreover, the displacements of the class IV_S strong relaxed rock mass in the left abutment are greater than those of the class IV_S strong relaxed rock mass in the right abutment.

Deformation characteristics during overloading process

Figure 9 illustrates the development processes of the radial displacements on the arch dam downstream surface, which

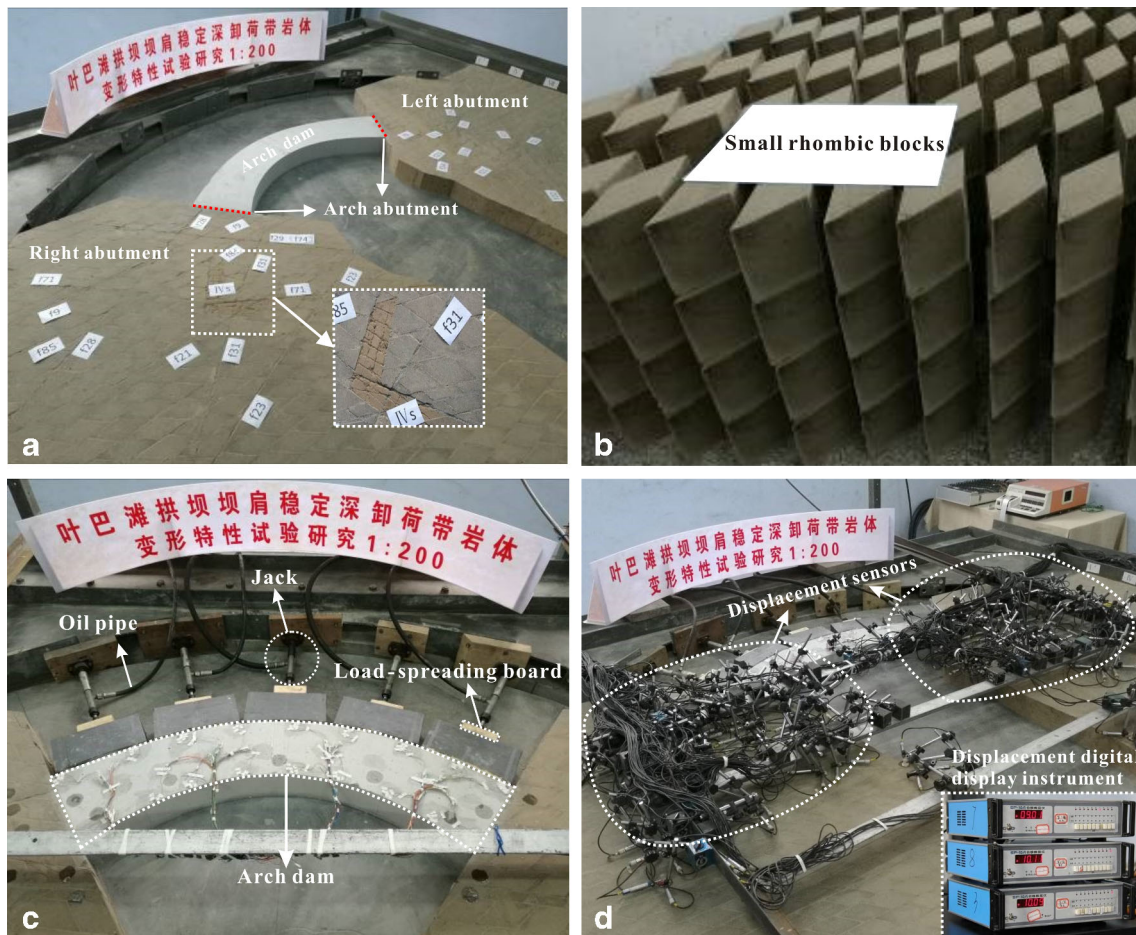


Fig. 5 Plane geomechanical model design of Yebatan arch dam. **a** Completed geomechanical model. **b** Small rhombic blocks for model masonry. **c** Loading system. **d** Displacement measuring system

increase with an increase in K_P . When K_P is relatively small, the displacements of the left and right half arches are symmetrical. When K_P is greater than 2.4, the displacement development of the left half arch is gradually faster than that of the right half arch. This indicates that the arch dam downstream deformation is accompanied by clockwise rotational

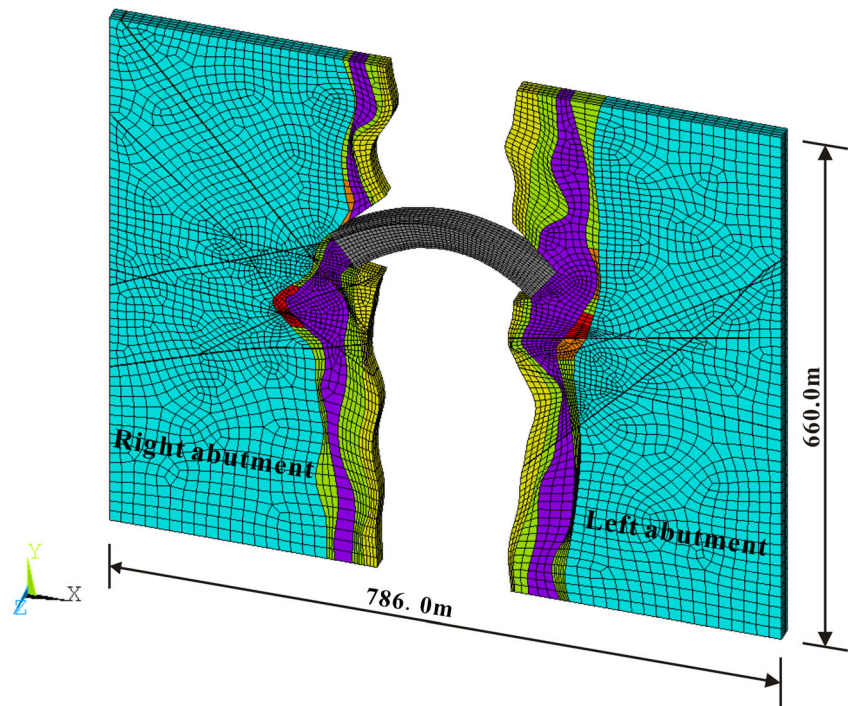
displacement. Eventually, the arch dam deformation is asymmetric, with a greater displacement of the left half arch than the right half arch.

During the overloading process, the displacements of the abutment increase with increased K_P (illustrated in Figs. 10 and 11). In the left abutment, the measuring points with large

Table 4 Main physical-mechanical parameters of the model material

Material		Density (g/cm ³)	Young's modulus (MPa)	Poisson's ratio	Cohesion (10 ⁻³ MPa)	Friction coefficient
Dam and rock mass	Concrete	2.40	165.0	0.170	18.75	1.50
	II ₁	2.73	92.5	0.220	8.50	1.28
	II ₂	2.73	77.5	0.220	6.00	1.20
	III ₁	2.65	60.0	0.260	5.50	1.08
	III ₂	2.65	45.0	0.280	4.50	0.95
	III _{2s}	2.65	17.5	0.280	4.25	0.86
	IV	2.55	12.5	0.330	3.00	0.70
	IV _s	2.55	5.0	0.330	2.50	0.60
Fault	f71	2.60	10.0	0.271	0.50	0.50
	f21 f22 f85 f9 f31	2.60	7.0	0.271	0.25	0.40
	f23 f24 f29(f74) f28	2.60	5.0	0.271	0.05	0.35

Fig. 6 FEM model of Yebatan arch dam and abutment



displacements are located in the area enclosed by the left arch abutment, fault f24 and deep-seated joint zone and in the right abutment is the area between fault f29 (f74) and the right arch abutment. These abutment displacement distribution characteristics are similar to those under a normal water load. However, the displacement developments of the measuring points near the two arch abutments are different. With an increase in K_B , the displacements along and across the river of the measuring points near the left arch abutment are gradually larger than those of the measuring points near the right abutment (i.e. the displacement of 9# is greater than 83#, and the displacement of 10# is greater than 84#). This indicates that the deformation of the two abutments becomes

asymmetric under overloading, which corresponds to the arch dam deformation. The arch dam and abutment deformation characteristics are not conducive to project operation and are closely related to the two large displacement areas in the abutment.

Under overloading, the areas with the largest displacement in the deep-seated joint zones are the same as those under normal water loads. However, the displacement differences of the class IV_S strong relaxed rock mass in the left and right abutments become increasingly obvious. The 23# and 24#, and 111# and 112# displacement sensors are installed to monitor the displacement of the class IV_S strong relaxed rock mass in the left and right abutments, respectively. The displacement

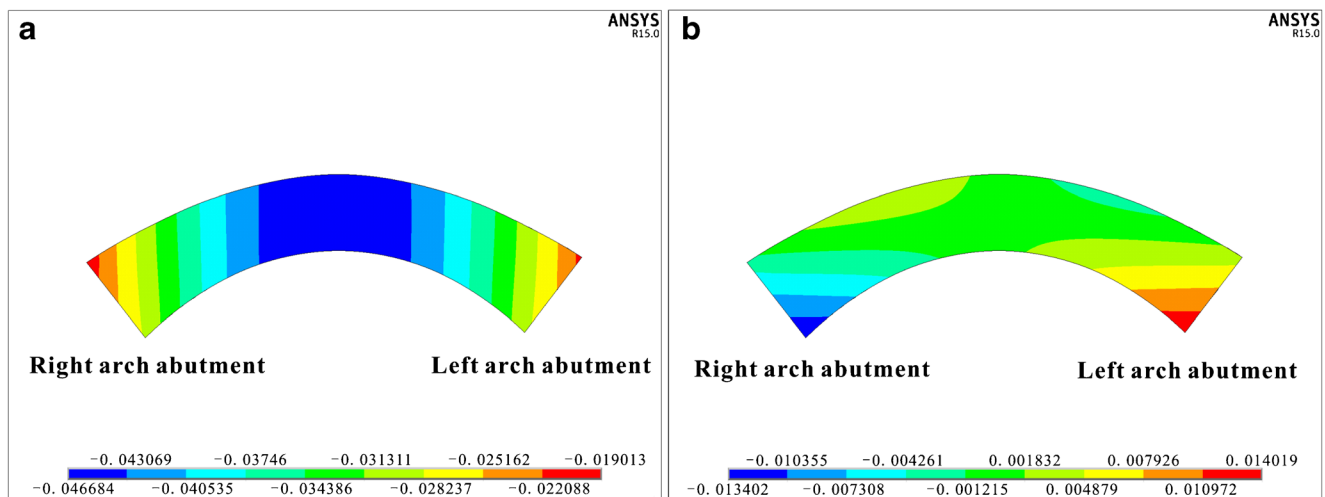


Fig. 7 Displacement contours of arch dam for $K_B = 1.0$ (unit: m). **a** Displacement along river. **b** Displacement across river (displacements along river and to right bank are defined as negative)

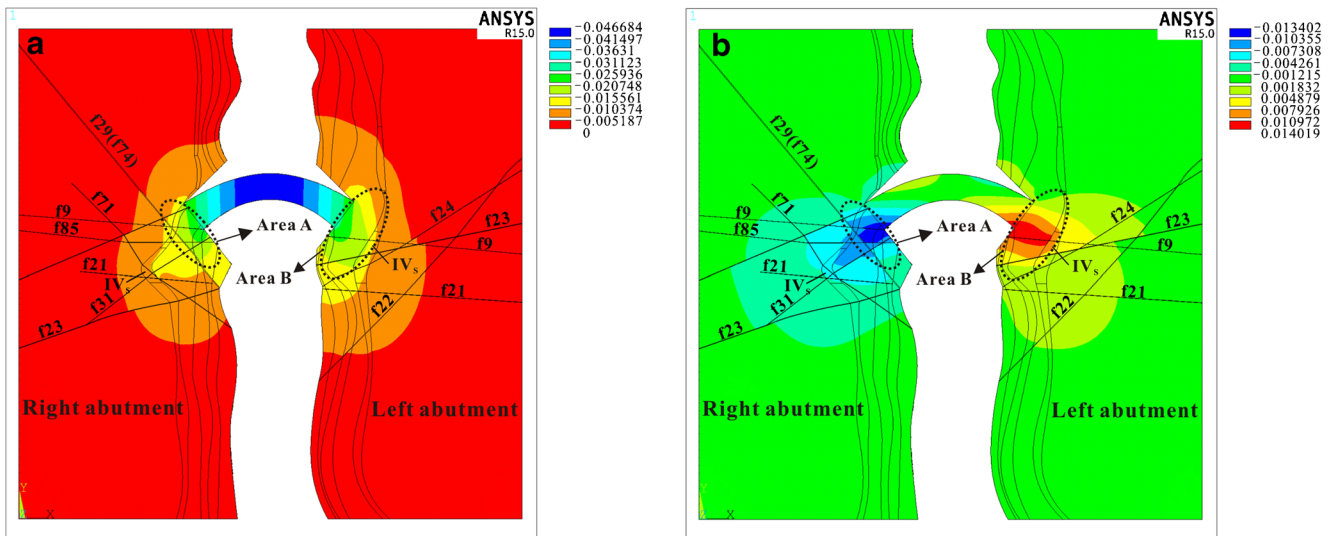


Fig. 8 Displacement contours of abutment for $K_p = 1.0$ (unit: m). **a** Displacement along river. **b** Displacement across river (displacements along river and to right abutment are defined as negative)

value variations of these displacement sensors demonstrate that the displacements of the class IV_S strong relaxed rock mass along and across the river in the left abutment are both larger than those of the class IV_S strong relaxed rock mass in the right abutment. This implies that the class IV_S strong relaxed rock mass in the left abutment exhibits higher displacement sensitivity with the upstream water load.

Furthermore, the displacement distributions in the arch thrust direction in both abutments exhibit similar characteristics. As illustrated in Fig. 12, significant displacement decrements occur in both abutment: one is in the class IV_S strong relaxed rock mass in the left abutment, and the other is in fault

f29 (f74) in the right abutment. The displacements downstream of the class IV_S strong relaxed rock mass in the left abutment and fault f29 (f74) in the right abutment are particularly small at each K_p , which means that the loads transmitted from the arch dam are significantly reduced by at these two geological structures.

Failure process and patterns

Figure 13 illustrates the plastic zone development in the FEM model. Plastic failures are initiated in the faults near the two arch abutments. And the rock mass near the dam heel enters the plastic failure stage (illustrated in Fig. 13a, b). With an increase in K_p , plastic zones develop at the rock mass near the dam toe. Furthermore, the plastic zones in two abutments are rapidly propagated in the downstream direction (illustrated in Fig. 13c). When $K_p = 4.0$, the plastic zones coalesce and form a large crack area in the left abutment, and the deep-seated joint zone experiences severe failure. Although a serious failure zone is formed near the right arch abutment, the plastic zones in the right abutment do not coalesce. The plastic failures in the two abutments are different. The failure degree of the left abutment is more serious than that of the right abutment (illustrated in Fig. 13d).

The geomechanical model cracking process is observed during the experiment. According to the observations, slight tensile cracks are initiated at the rock mass near the dam heel (illustrated in Fig. 14a), and the model exists in the elastic deformation stage under a normal water load. With the increase in K_p , the cracks near the dam heel gradually propagate towards both banks (shown in Fig. 14b). Furthermore, the rock mass near the dam toe begins to fracture. Cracks also occur in the faults near the two arch abutments, such as faults

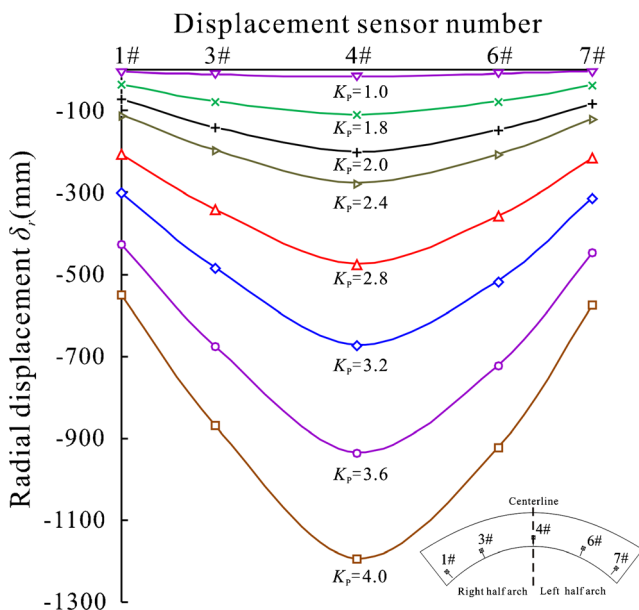


Fig. 9 Distribution curves of radial displacement on downstream arch dam surface at EL. 2750 m (pointing to downstream is negative)

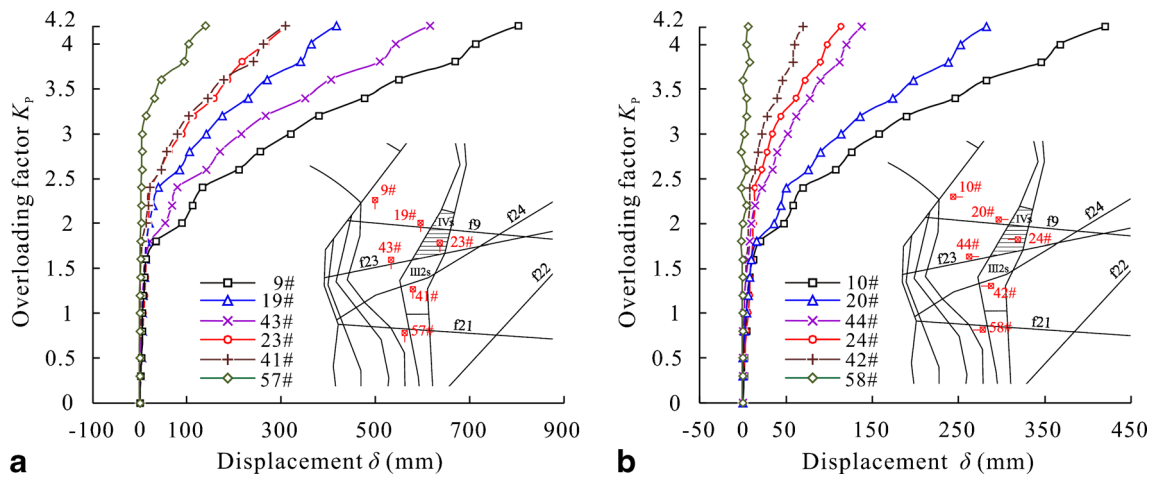


Fig. 10 Curves of displacement δ vs. overloading factor K_p in left abutment. **a** Displacement along river (pointing to downstream is positive). **b** Displacement across river (pointing to each bank is positive)

f29 (f74), f9 and f23 (shown in Fig. 14c). Most cracks occur and propagate during the period when $K_p = 3.0\text{--}4.0$, and the dam structures approached the limitation. In particular, the cracks in the left abutment are extended to the deep-seated joint zone. In general, the development process and distribution of the asymmetric cracking zones are similar to the numerical results, both of which indicate that the load-bearing capacity of the left abutment is inferior to that of the right abutment.

The final failure patterns of the geomechanical model are illustrated in Fig. 14d, where the two abutments exhibit different failure patterns. Near the left arch abutment, the rock mass and faults f9, f23 and f24 are severely cracked. Moreover, cracks occur in the class IV_S strong relaxed rock mass. In the right abutment, the rock mass between fault f29 (f74) and the arch abutment, and faults f9, f28, f31 and f85 are seriously cracked. A near-triangle failure zone is ultimately formed in the left abutment, and a strip-shaped

failure zone is observed near the right arch abutment. It is worth noting that significant slippage is observed at fault f29 (f74). The arch thrust causes severe shear failure in fault f29 (f74), resulting in it to form a sliding surface for the rock mass near the right arch abutment. Thereafter, the rock mass near the right abutment is slipped in the downstream direction along fault f29 (f74).

Discussion

Rock mechanical properties' effect on deformation

The abutment deformation is closely related to the mechanical properties of the abutment rock mass (Lin et al. 2015). Rock masses with low rigidity and poor structural integrity near arch abutments often lead to an excessive arch dam and abutment deformation (Zhang et al. 2014). In the left

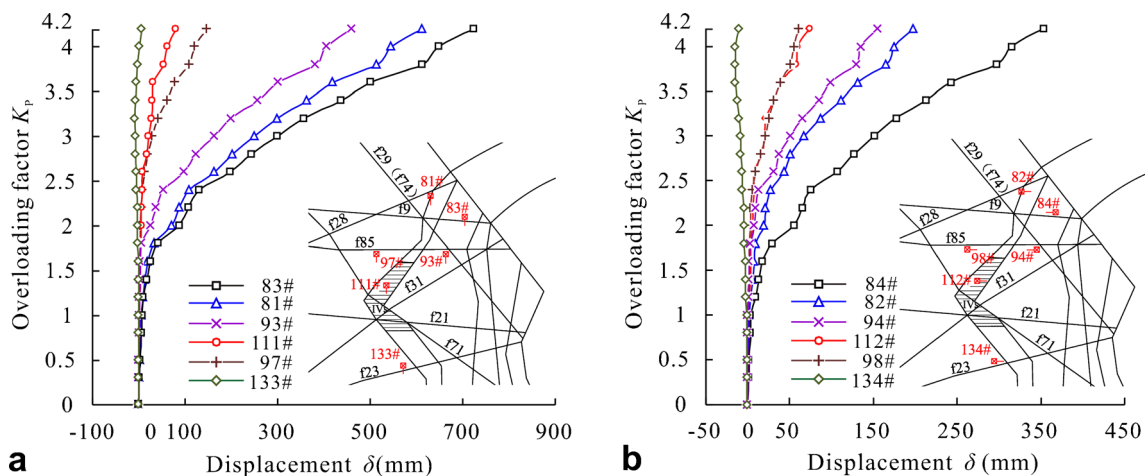


Fig. 11 Curves of displacement δ vs. overloading factor K_p in right abutment. **a** Displacement along river (pointing to downstream is positive). **b** Displacement across river (pointing to each bank is positive)

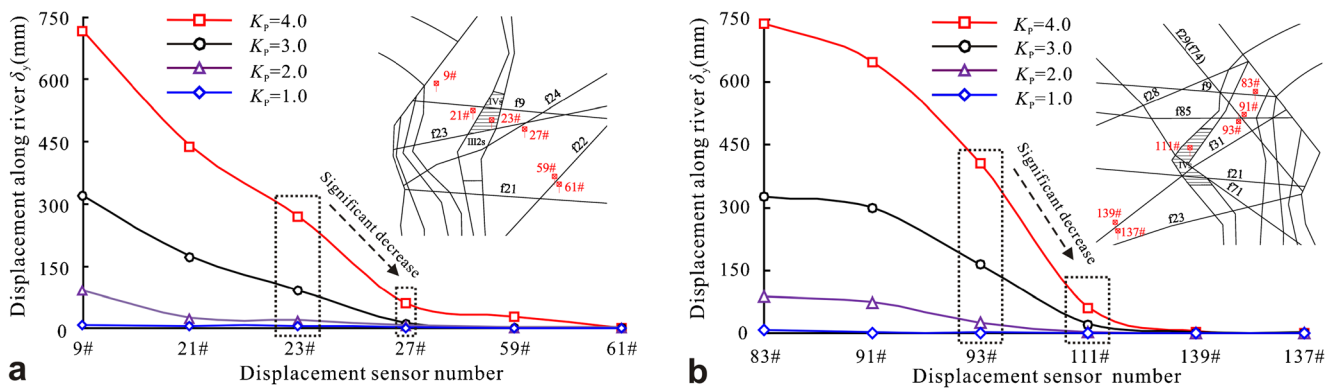


Fig. 12 Displacement distribution along the arch thrust transmission direction. **a** Measuring points in left abutment. **b** Measuring points in right abutment

abutment of the Yebatan arch dam, the class IV_S strong relaxed rock mass in the deep-seated joint zone is close to the arch abutment. And it is situated in the transmission direction of the arch thrust. The rock mass between the

deep-seated joint zone and the arch abutment belongs to class II₂. The class II₂ rock mass exhibits high rigidity and strong integrity. Its Young's modulus is approximately 12.0–19.0 GPa, and the fault development degree is low.

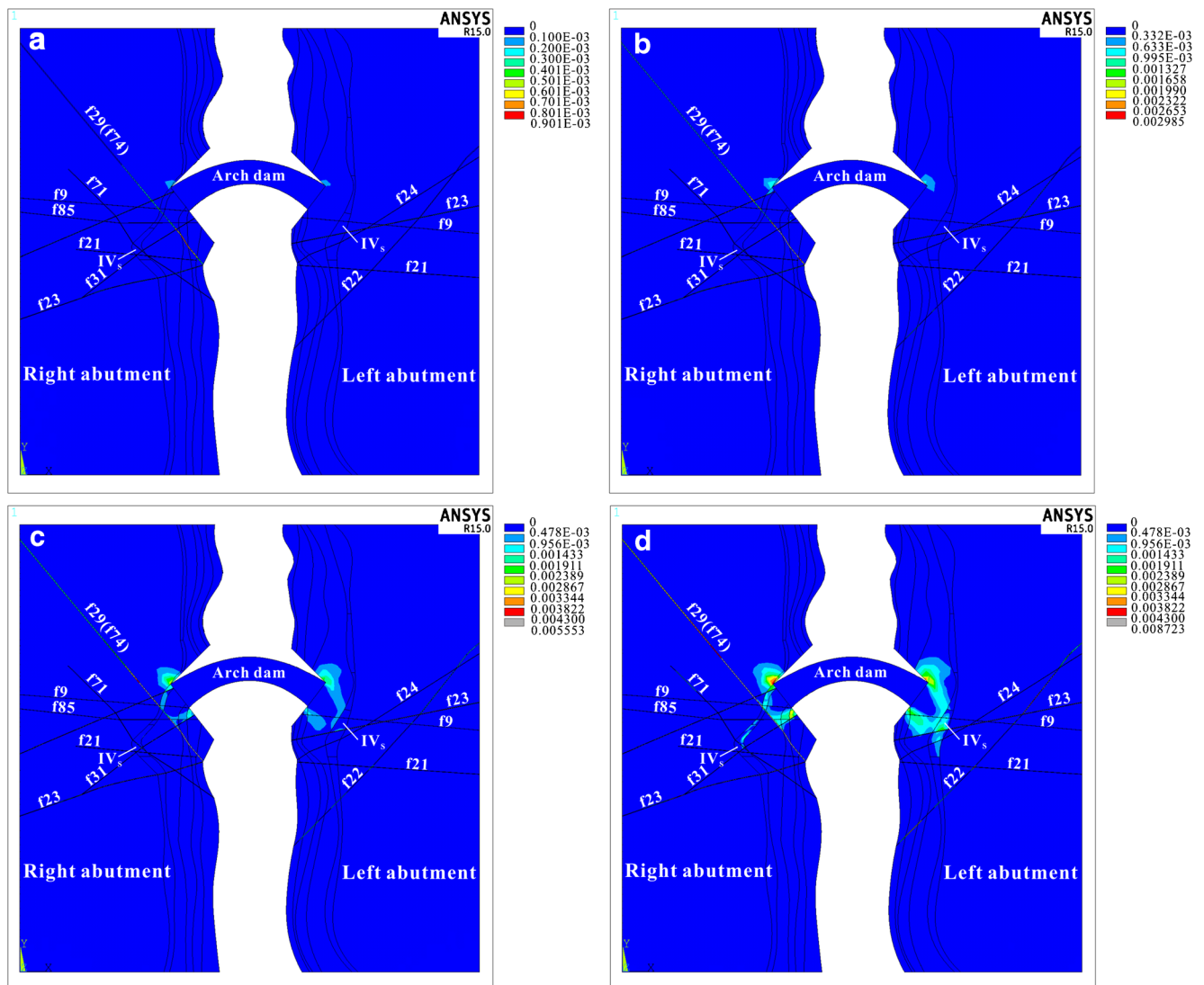


Fig. 13 Plastic strain in FEM model under overloading. **a** $K_p = 1.0$. **b** $K_p = 2.0$. **c** $K_p = 3.0$. **d** $K_p = 4.0$

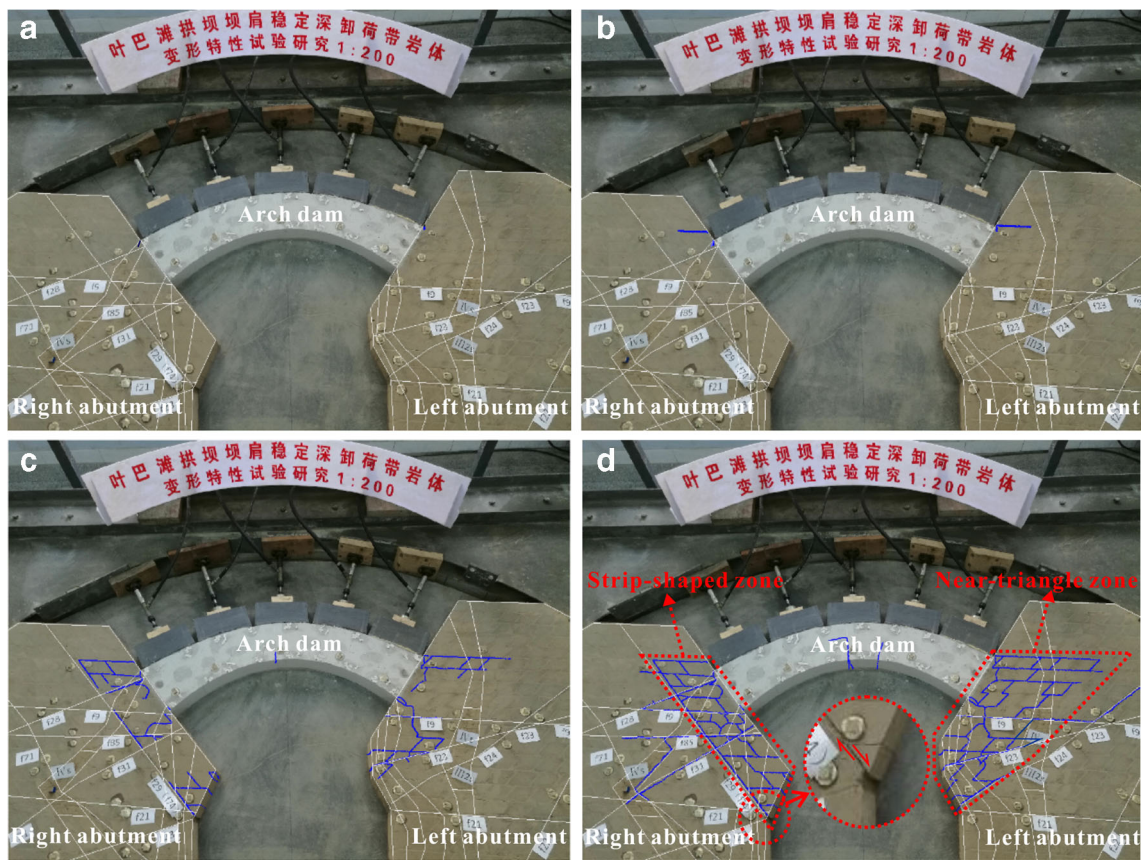


Fig. 14 Cracking process of geomechanical model during overloading process. **a** $K_p=1.0$. **b** $K_p=2.0$. **c** $K_p=3.0$. **d** $K_p=4.0$ (blue lines represent cracks)

However, the Young's modulus of the class IV_S strong relaxed rock mass is relatively small, at approximately 1.0 GPa, and the rock mass is severely fractured. There is a parametric mutation in the Young's modulus of the abutment rock mass. This mutation has an adverse effect on the abutment deformation. Under the action of the arch thrust, the class IV_S strong relaxed rock mass is severely compressed, and the displacement of the class II_2 rock mass and arch dam is significantly increased. The arch thrust energy is dissipated extensively during the compression process of the class IV_S strong relaxed rock mass. Therefore, the arch thrust action on the rock mass downstream of the class IV_S strong relaxed rock mass is significantly reduced. In general, the deformation of arch dam and abutment increases significantly due to the poor mechanical properties of the class IV_S strong relaxed rock mass in the left abutment. This rock mass also has an obvious reducing effect on the load transmission.

Fault reducing effect

According to the above discussion, the deep-seated joint zone has a significant effect on the arch dam and abutment working

performance. However, under certain special geological conditions, such as severely developed faults in the abutment, the effect degree of the deep-seated joint zone may be different. In the right abutment, the rock mass between fault f29 (f74) and the right arch abutment is severely cut by the faults, thereby reducing its integrity and bearing capacity. Under a huge arch thrust, the displacement of the rock mass at this zone is relatively large. Moreover, fault f29 (f74) is near the right arch abutment with a downstream strike. Under the arch thrust action, fault f29 (f74) is severely cracked and formed a sliding plane. The stability of the right abutment is seriously affected. Furthermore, the arch thrust energy is released along with the rock mass sliding to the downstream surface. Fault f29 (f74) plays a dominant role in controlling the anti-sliding stability of the right abutment and reducing the arch thrust transmission. The class IV_S strong relaxed rock mass in the right abutment is located downstream of fault f29 (f74), the arch thrust effect on the class IV_S rock mass is obviously reduced and the displacement of the class IV_S strong relaxed rock mass is relatively small. Consequently, the adverse impact of the class IV_S strong relaxed rock mass is less than that of fault f29 (f74) in the right abutment. This is the reducing effect caused by the combination of faults. In general, fault f29 (f74) has the

dominant adverse effect on the arch dam and abutment working performance and reduces the effect degree of the deep-seated joints accordingly.

Reinforcement measures

It is revealed that the class IV_S strong relaxed rock mass in the left abutment and fault f29 (f74) in the right abutment are the project weaknesses. To improve the arch dam and abutment working performance, certain reinforcement measures should be proposed accordingly. According to the reinforcement measures adopted by other similar high arch dam projects, the concrete replacement measure is usually employed as the primary foundation reinforcement measure to treat the adverse geological structures (Li et al. 2012; Shapira 2015). As illustrated in Fig. 15, the class IV_S strong relaxed rock mass in the left abutment is excavated and replaced by concrete to improve the left abutment and left half arch deformation performance. Moreover, fault f29 (f74) is locally excavated and replaced by a shear hole to increase the shear resistance capacity. The mechanical parameters of the replacement concrete are displayed in Table 5. Based on the reinforcement scheme, an additional FEM calculation is carried out to study the arch dam and abutment working performance following reinforcement. The FEM calculation process prior to and after reinforcement is similar.

The failure and deformation characteristics of the arch dam and abutment prior to and after reinforcement are obviously different. Following reinforcement, the plastic zone propagation range in the left abutment decreases significantly, and the plastic failure degree in fault f29 (f74) is obviously reduced. When $K_p = 4.0$, the plastic zones in the two abutments do not coalesce (illustrated in Fig. 16a). Moreover, the replacement concrete prevents the plastic zone from continuing to propagate downstream in the left

abutment, while the shear hole obstructs the plastic zone in fault f29 (f74) from extending further downstream. The failure degrees of the two abutments are significantly reduced. The final failure state of the FEM model is illustrated in Fig. 16b. The areas with severe plastic failure in the left abutment are mainly located between the deep-seated joint zone and left arch abutment, which indicates the plastic zone range in the left abutment is obviously narrowed. Correspondingly, fault f29 (f74) in the right abutment experiences local plastic failure and does not penetrate to the downstream free surface. This indicates that fault f29 (f74) is not formed a sliding plane for the rock mass near the left arch abutment.

As the reinforcement measures increase the abutment rigidity, the arch dam and abutment deformation performance are improved. Figure 16c, d illustrates the displacement distributions of the FEM model following reinforcement. The displacements near the left and right arch abutments can be observed to be similar, indicating that the asymmetrical deformation of the arch dam and abutment is improved. Moreover, the distribution of the large displacement area in the two abutments is basically the same, and the large displacement area in the left abutment shrinks as a result of the replacement concrete.

Figure 17 illustrates the stress states of the FEM model prior to and after reinforcement. Before reinforcement, the dam stress is mainly composed of compressive stress, with local tensile stress zones on the dam heel and downstream surface. And in left abutment, the stress distribution near the class IV_S strong relaxed rock mass is discontinuous. After reinforcement, the stress states of the arch dam and abutment are locally improved. The stress distribution of the arch dam exhibits strong symmetry after reinforcement, and the tensile stress range on the downstream surface is narrowed. Furthermore, the maximum principal stress at dam heel is reduced from 1.85~2.25 to 1.44~1.85 MPa.

Fig. 15 Schematic of reinforcement

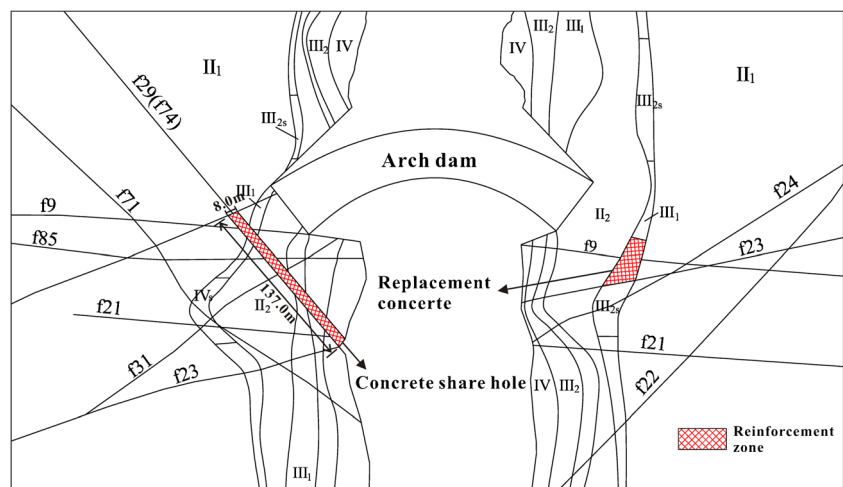


Table 5 Physical-mechanical parameters of replacement concrete

Density (g/cm ³)	Young's modulus (GPa)	Poisson's ratio	Cohesion (MPa)	Friction coefficient
2.40	33.0	0.170	3.50	1.50

Besides, the compressive stress near the deep-seated joint zone in the left abutment is uniformly distributed due to the class IV_S strong relaxed rock mass is excavated and replaced by concrete.

The above calculation results demonstrate that the reinforced abutment rigidity and strength are obviously improved, which is reflected in eliminating the arch dam and abutment deformation asymmetry, improving the overloading capacity and increasing the shear resistance capacity of fault f29 (f74). Moreover, the stress states of the arch dam and abutment are locally improved. This demonstrates that the concrete

replacement measure is feasible for improving the arch dam and abutment working performance. These research results can provide an important scientific insight for the engineering reinforcement of this project.

Conclusions

In this study, the Yebatan arch dam was considered as a typical high arch dam with the geological defect of deep-seated joints. Both geomechanical model test and numerical analysis were

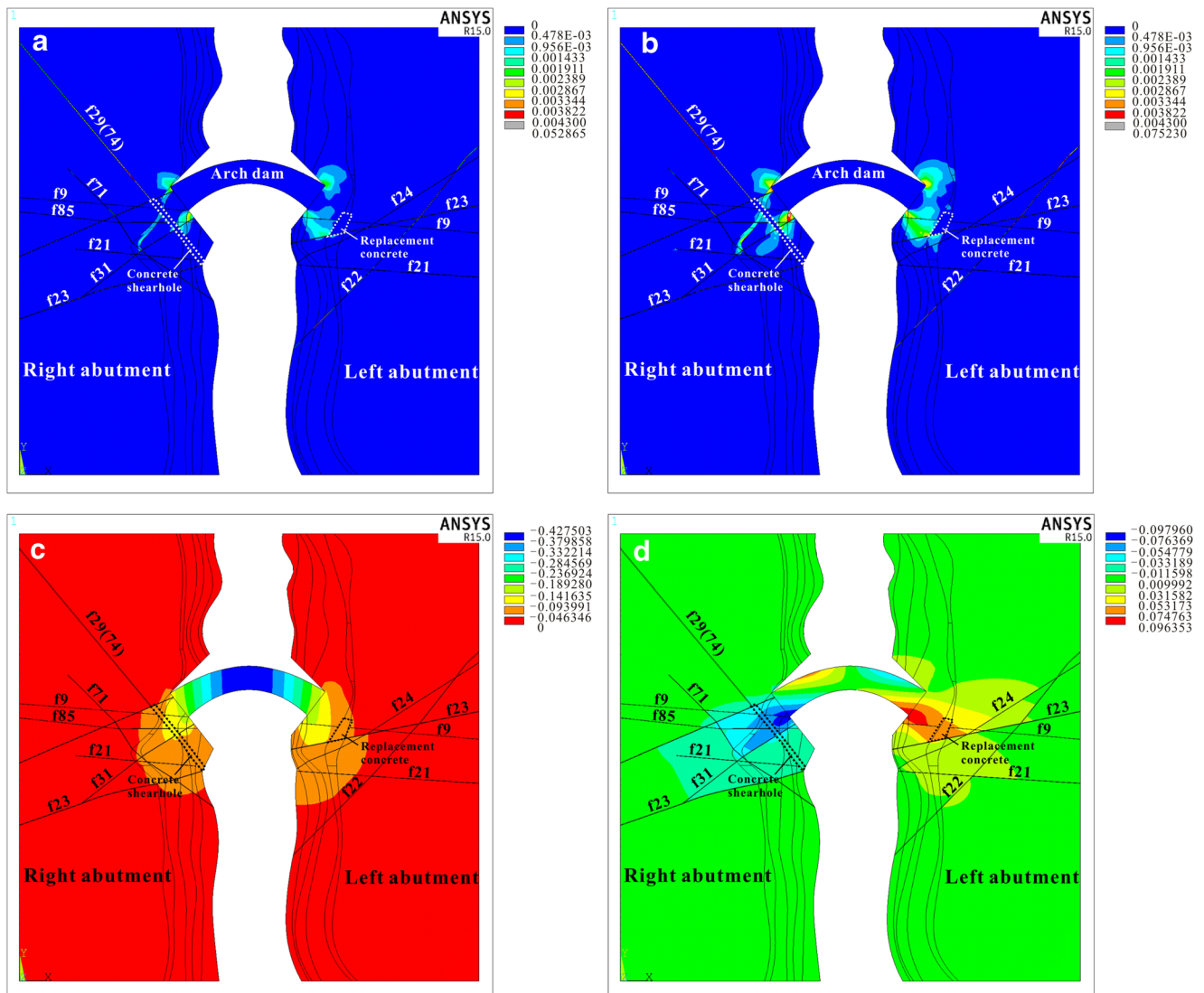


Fig. 16 FEM calculation results for reinforced abutment. **a** Plastic strain for $K_p = 4.0$. **b** Plastic strain final state. **c** Displacement along river for $K_p = 4.0$ (unit: m). **d** Displacement across river for $K_p = 4.0$ (unit: m) (displacements along river and to right abutment are defined as negative)

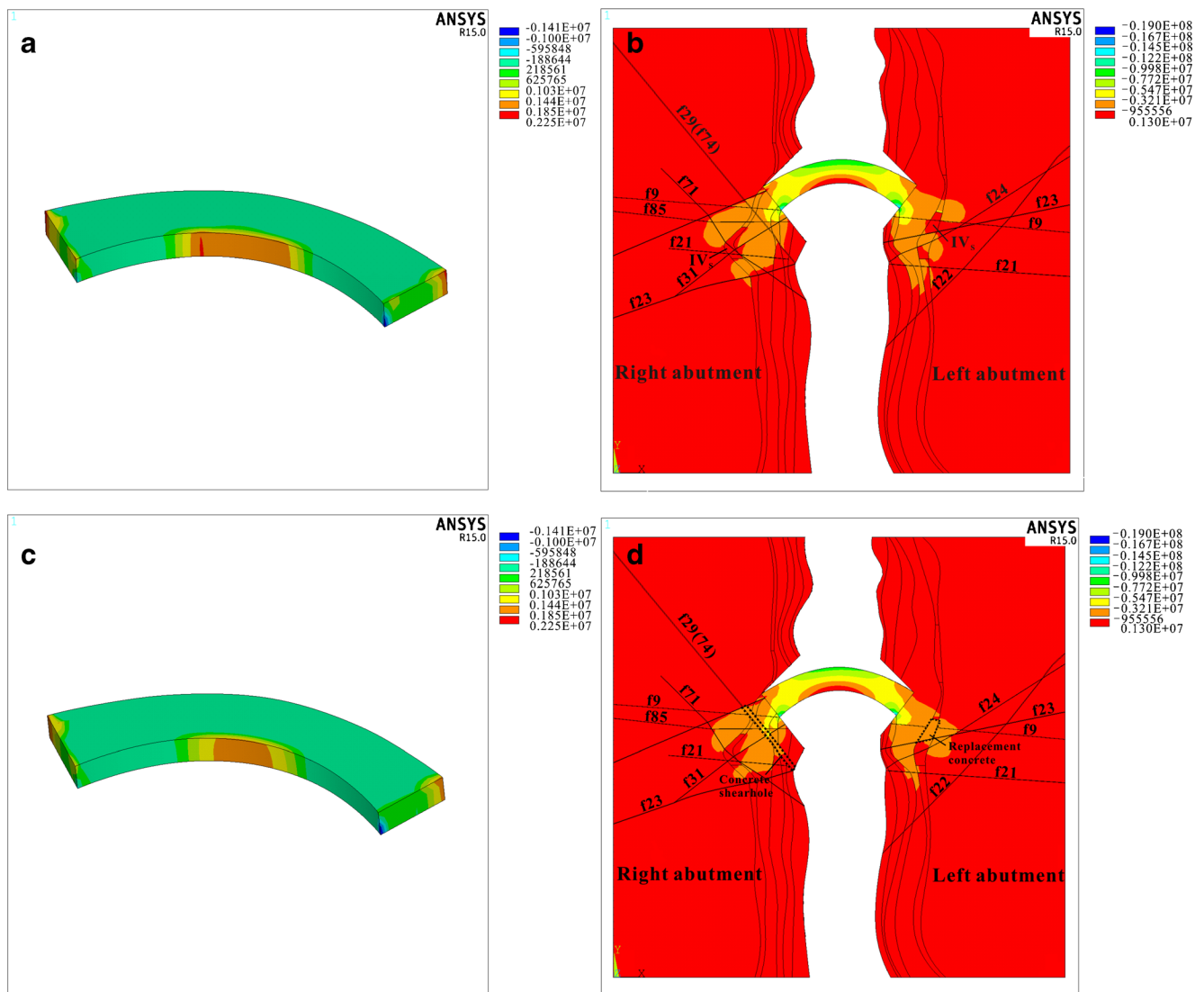


Fig. 17 Stress distribution characteristics of arch dam and abutment as $K_p = 1.0$ (unit: Pa). **a** Maximum principal stress before reinforcement. **b** Minimum principal stress before reinforcement. **c** Maximum principal stress after reinforcement. **d** Minimum principal stress after reinforcement

carried out to study the effect of deep-seated joints on the arch dam and abutment working performance. Based on the experimental and numerical analysis results, the following conclusions can be drawn.

- (1) Under the normal water load, the deformation and failure degree of the arch dam and abutment are within the acceptable range. During the overloading process, asymmetrical deformation of the arch dam and abutment occurs, and the rock mass near the right arch abutment slides along fault f29 (f74).
- (2) Two critical areas with large displacement and serious cracking are revealed in the abutment. One is the near-triangle area enclosed by the left arch abutment, the deep-seated joint zone and fault f24. The other one is the strip-shaped area between fault f29 (f74) and the right arch abutment.
- (3) The deep-seated joint zones have a significant effect on the arch dam and abutment working performance. The effect degree is strongly dependent on the location of the class IV_S strong relaxed rock mass and the combination with faults.
- (4) The displacements of the arch dam and the left abutment increase obviously due to the poor mechanical properties of the class IV_S strong relaxed rock mass in the left abutment. Fault f29 (f74) has a dominant adverse effect on the right abutment stability and reduces the effect degree of the deep-seated joints in the right abutment accordingly.
- (5) After treating by concrete replacement measures, the deformation asymmetry of the arch dam and the abutment is effectively eliminated, and the anti-sliding stability of the right abutment is improved. This kind of reinforcement measure is feasible to improve the arch dam and abutment working performance.

This study provides a scientific basic for the design, stability evaluation and dam foundation treatment of the Yebatan arch dam. Meanwhile, this study provides a reference for other similar high arch dam projects. Considering that this study is performed by a single-factor method (overloading method), it needs a further study under multi-factor coupling (i.e. spatial variability of the jointed rock masses, creep characteristics of jointed rock masses).

Funding information This work was supported by the National Key R&D Program of China (Grant No. 2016YFC0401908) and the National Natural Science Foundation of China (Grant No. 51609163).

References

- Alejano LR (2012) Drucker–Prager criterion. *Rock Mech Rock Eng* 45(6):995–999
- Barla G, Antolini F, Barla M, Mensi E, Piovano G (2010) Monitoring of the Beaugard landslide (Aosta Valley, Italy) using advanced and conventional techniques. *Eng Geol* 116(3–4):218–235
- Chen Y, Zhang L, Yang GX, Dong JH, Chen JY (2012) Anti-sliding stability of a gravity dam on complicated foundation with multiple structural planes. *Int J Rock Mech Min Sci* 55(10):151–156
- Chen Y, Zhang L, Yang BQ, Dong JH, Chen JY (2015) Geomechanical model test on dam stability and application to Jinping high arch dam. *Int J Rock Mech Min Sci* 76:1–9
- Drucker DC, Prager W (2013) Soil mechanics and plastic analysis or limit design. *Qapmath* 10(2):157–165
- Fei WP, Zhang L, Zhang R (2010) Experimental study on a geomechanical model of a high arch dam. *Int J Rock Mech Min Sci* 47(2):299–306
- Fumagalli IE (1973) *Statical and geomechanical models*. Springer, New York
- Guo LN, Li TC, Lu SS, Guo YJ (2011) Deep sliding stability analysis of gravity dam based on FEM strength reduction. *Adv Mater Res* 243–249:4608–4613
- Hennig T, Wang W, Feng Y, Ou X, He D (2013) Review of Yunnan’s hydropower development. Comparing small and large hydropower projects regarding their environmental implications and socio-economic consequences. *Renew Sust Energ Rev* 27:585–595
- Lan HX, Wu FQ, Yan FZ, Qi SW (2004) Mechanism of deep cracks in the left bank slope of Jinping first stage hydropower station. *Eng Geol* 73(1):129–144
- Li SQ, Li ZN, Li GQ, Mengd JF, Tang J (2005) Experimental and numerical seismic investigations of the Three Gorges dam. *Eng Struct* 27:501–513
- Li N, Yao XC, Qu X, Zhang CK, Zhang ZQ, Zhou Z (2012) Strengthening treatment and analysis for the left bank abutment of Jinping arch dam. *Geomechanik Und Tunnelbau* 5(5):497–502
- Lin P, Ma TH, Liang ZZ, Tang CA, Wang RK (2014) Failure and overall stability analysis on high arch dam based on DFPA code. *Eng Fail Anal* 45(1):164–184
- Lin P, Liu XL, Zhou WY, Wang RK, Wang SY (2015) Cracking, stability and slope reinforcement analysis relating to the Jinping dam based on a geomechanical model test. *Arab J Geosci* 8(7):4393–4410
- Lin P, Shi J, Zhou WY, Wang RK (2018) 3D geomechanical model tests on asymmetric reinforcement and overall stability relating to the Jinping I super-high arch dam. *Int J Rock Mech Min Sci* 102:28–41
- Liu YR, Guan FH, Yang Q, Yang RQ, Zhou WY (2013) Geomechanical model test for stability analysis of high arch dam based on small blocks masonry technique. *Int J Rock Mech Min Sci* 61:231–243
- Liu JS, Ding WL, Yang HM, Wang RY, Yin S, Li A, Fu FQ (2017a) 3D geomechanical modeling and numerical simulation of in-situ stress fields in shale reservoirs: a case study of the lower Cambrian Niutitang formation in the Cen’gong block, South China. *Tectonophysics* 712–713:663–683
- Liu, LJ, Zhao QH, Han, G (2017b) Characteristics of deep-seated crack in dam site of Yebatan hydropower station. *Chin J Geotech Eng* 39(3): 501–508 [in Chinese]
- Pan JZ, He J (2000) *Fifty years of Chinese dam*. China Water Power Press, Beijing [in Chinese]
- Ren QW, Li Q, Liu S (2012) Research advance in failure risk and local strength failure for high arch dams. *Sci Bull* 57(36):4672–4682
- Shapira J (2015) Efficient 3-D reliability analysis of the 530 m high abutment slope at Jinping I hydropower station during construction. *Eng Geol* 195(11):269–281
- Song SW, Feng XM, Xiang BY, Xing WB, Zeng Y (2011) Research on key technologies for high and steep rock slopes of hydropower engineering in southwest China. *Chin J Rock Mech Eng* 30(1):1–22 [in Chinese]
- Song ZH, Liu YR, Yang Q (2015) Experimental and numerical investigation on the stability of a high arch dam with typical problems of nonsymmetry: Baihetan dam, China. *B Eng Geol Environ* 75(4):1–16
- Sun GH, Zheng H, Liu DF (2011) A three-dimensional procedure for evaluating the stability of gravity dams against deep slide in the foundation. *Int J Rock Mech Min Sci* 48(3):421–426
- Wang GJ, Xie MW, Chai XQ, Dong CX (2013) D-InSAR-based landslide location and monitoring at Wudongde hydropower reservoir in China. *Environ Earth Sci* 69(8):2763–2777
- Yang BQ, Zhang L, Liu EL, Dong JH, Zhu HH, Chen Y (2015) Deformation monitoring of geomechanical model test and its application in overall stability analysis of a high arch dam. *J Sensors* 2015(5):1–12
- Yin Y, Huang B, Wang S, Li J (2015) Potential for a Ganhaizi landslide-generated surge in Xiluodu Reservoir, Jinsha River, China. *Environ Earth Sci* 73(7):3187–3196
- Zhang L, Chen Y, Yang BQ, Dong JH, Chen JY (2009) *Hydraulic model test of dam and foundation and its engineering application*. Sichuan University Press, Chengdu [in Chinese]
- Zhang L, Liu YR, Yang Q, Yang RQ (2014) Research on geomechanical model test of Dagangshan high arch dam based on block masonry technique. *Engineering Mechanics* 17(8):695–703 [in Chinese]
- Zhang L, Liu YR, Yang Q (2015) Evaluation of reinforcement and analysis of stability of a high-arch dam based on geomechanical model testing. *Rock Mech Rock Eng* 48(2):803–818
- Zhou W, Chang XL, Zhou CB, Liu XH (2008a) Failure analysis of high-concrete gravity dam based on strength reserve factor method. *Comput Geotech* 35(4):627–636
- Zhou WY, Lin P, Yang Q, Yang RQ, Zhou Z (2008b) Experimental research on stability of Jinping high slope with three-dimensional geomechanical model. *Chin J Rock Mech Eng* 27(5):893–901 [in Chinese]
- Zhu WS, Zhang QB, Zhu HH, Li Y, Yin JH, Li SC, Sun LF, Zhang L (2010) Large-scale geomechanical model testing of an underground cavern group in a true three-dimensional (3-D) stress state. *Can Geotech J* 47:935–946
- Zhu HE, Liu YR, Pan YW, Qiang Y (2015) Evaluating the safety of high arch dams with fractures based on numerical simulation and geomechanical model testing. *Sci China Technol Sc* 58(10):1648–1659
- Zuo QD (1984) *The theory and method of model test*. Water Resources and Electric Power Press, Beijing [in Chinese]